SANDIA REPORT

SAND 2005-7118
Unlimited Release
Printed November 2005

Final Report on LDRD Project: Leaky-mode VCSELs for photonic logic circuits

Darwin K. Serkland, Kent M. Geib, Gregory M. Peake, G. Ronald Hadley, Terry W. Hargett, Andrea T. Ongstad, Victoria M. Montano, Gordon A. Keeler, Ethan L. Blansett, Thomas M. Bauer, Melissa R. Medrano, Charles T. Sullivan

Prepared by
Sandia National Laboratories
Albuquerque, New Mexico 87185 and Livermore, California 94550

Sandia is a multiprogram laboratory operated by Sandia Corporation, a Lockheed Martin Company, for the United States Department of Energy's National Nuclear Security Administration under Contract DE-AC04-94AL85000.

Issued by Sandia National Laboratories, operated for the United States Department of Energy by Sandia Corporation.

Available to DOE and DOE contractors from
U.S. Department of Energy
Office of Scientific and Technical Information
P.O. Box 62
Oak Ridge, TN 37831

Telephone: (865)576-8401
Facsimile: (865)576-5728
E-Mail: reports@adonis.osti.gov
Online ordering: http://www.osti.gov/bridge

Available to the public from
U.S. Department of Commerce
National Technical Information Service
5285 Port Royal Rd
Springfield, VA 22161

Telephone: (800)553-6847
Facsimile: (703)605-6900
E-Mail: orders@ntis.fedworld.gov
Online order: http://www.ntis.gov/help/ordermethods.asp?loc=7-4-0#online

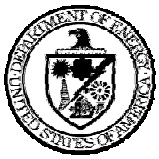

SAND2005-7118
Unlimited Release
Printed November 2005

Final Report on LDRD Project: Leaky-mode VCSELs for photonic logic circuits

Darwin K. Serkland, Kent M. Geib, Gregory M. Peake, G. Ronald Hadley, Terry W. Hargett, Andrea T. Ongstad[*], Victoria M. Montano[*], Gordon A. Keeler, Ethan L. Blansett, Thomas M. Bauer[*], Melissa R. Medrano, Charles T. Sullivan
RF Microsystems Technologies Department

Sandia National Laboratories
P. O. Box 5800
Albuquerque, New Mexico 87185-0603

Abstract

This report describes the research accomplishments achieved under the LDRD Project "Leaky-mode VCSELs for photonic logic circuits." Leaky-mode vertical-cavity surface-emitting lasers (VCSELs) offer new possibilities for integration of microcavity lasers to create optical microsystems. A leaky-mode VCSEL output-couples light laterally, in the plane of the semiconductor wafer, which allows the light to interact with adjacent lasers, modulators, and detectors on the same wafer. The fabrication of leaky-mode VCSELs based on effective index modification was proposed and demonstrated at Sandia in 1999 but was not adequately developed for use in applications. The aim of this LDRD has been to advance the design and fabrication of leaky-mode VCSELs to the point where initial applications can be attempted. In the first and second years of this LDRD we concentrated on overcoming previous difficulties in the epitaxial growth and fabrication of these advanced VCSELs. In the third year, we focused on applications of leaky-mode VCSELs, such as all-optical processing circuits based on gain quenching.

[*] L&M Technologies, Inc.

Acknowledgments

The authors acknowledge professor Kent D. Choquette for starting the leaky mode VCSEL experimental effort at Sandia and for encouraging us to further develop this technology. We thank G. Allen Vawter and Weng W. Chow for discussions of their work on gain quenched lasers. We thank L. Bao and professor Luke Mawst for helpful discussions of leaky mode VCSEL arrays. We thank Daniel M. Grasso and professor Kent D. Choquette for collaboration on coupled-cavity VCSEL research. We thank Preetpaul Devgan and professor Prem Kumar for collaboration on VCSEL-based opto-electronic oscillators. We also thank John Nogan for helping us to modify the PlasmaTherm 790 PECVD tool for automated dielectric DBR deposition. We gratefully acknowledge the expert technical assistance that was provided by Gary D. Karpen. Sandia is a multiprogram laboratory operated by Sandia Corporation, a Lockheed Martin Company, for the United States Department of Energy's National Nuclear Security Administration under contract DE-AC04-94AL85000.

Contents

(This page is left blank intentionally.)

1. Introduction

1.1. LDRD Project Overview

The development of all-optical-logic circuits that can process data directly in the optical domain will enable front-end processing of optical data at very high bit rates (>40Gbit/sec) with minimal latency, on the order of a few bit periods. Such high-speed all-optical processing nodes will initially be sought for optical fiber networks, enabling high-speed data encryption, decryption, and packet routing, and will eventually be sought to improve the performance of distributed-processor supercomputers. One promising all-optical-logic technology that has been pursued utilizes gain quenching of an edge-emitting laser caused by injected light from another laser. We proposed for this LDRD project to investigate gain quenching of vertical-cavity surface-emitting lasers (VCSELs) using novel leaky-mode microcavity concepts that were pioneered at Sandia.

Leaky-mode techniques, first proposed at Sandia in 1995 and validated by a phase-locking experiment in 1999, allow VCSELs to output light laterally (in the plane of the semiconductor wafer). Hence, the output of one laser can be laterally injected into other lasers to achieve interconnection of optical circuits. Moreover, VCSELs have significant advantages over edge-emitting lasers, including smaller size and lower power consumption, allowing higher density integration without severe heating limitations, and higher relaxation oscillation frequencies, allowing operation at faster clock speeds. We at Sandia are in a unique position, with expertise in theory, design, growth, fabrication, and characterization, to develop this potentially revolutionary microcavity laser logic technology.

1.2. Technical Problem and Approach

Future secure data transmission and high-speed computing systems could greatly benefit by the availability of high-speed (>40Gbit/sec) logic circuits that can do front-end processing of digital data traveling through optical fibers. The goal is not to replace conventional electronic logic circuits, but rather to implement limited functionality all-optical logic circuits for use in optical communication links, where optical “transparency” and high speed are of paramount importance. The first problem to be addressed is the demonstration of a single very fast all-optical logic gate that exhibits minimum power dissipation and maximum optical gain. The second problem to be addressed is the integration of several such logic gates to achieve an optical integrated circuit. The chosen logic gate technology must be compatible with microfabrication techniques, in order to meet the eventual need for integration into dense optical circuits. Roughly 100 gates must be integrated to meet the functionality requirements of a typical front-end optical processing circuit.

Vertical-cavity surface-emitting lasers (VCSELs) have been identified as a natural candidate for laser logic gates, due to their promise of low power consumption and high speeds. Until recently, however, an effective method for transporting light between lasers was still unknown since propagation in VCSELs is normal to the wafer. The discovery of

the effective index method for waveguiding in VCSELs and its application to leaky-mode coupling between VCSELs has provided such a method. Changes in effective index are engineered by constructing channels of increased (vertical) cavity length, indicated by the gray region in Figure 1.1(a). In these channels, light propagates with a tilted propagation vector, as shown in Figure 1.1(b) that is still mostly normal to the wafer plane, but tilted enough so that light "walks" down the channel. Such a scheme has been demonstrated at Sandia, where a high-index channel was employed to couple together two VCSELs separated by as much as 20 microns, as shown in Figure 1.2. We propose to use similar channels to transport light from one VCSEL to another, where it may be used to quench the gain of the second laser and turn off its free-running mode. If the second laser is similarly connected to other lasers, a series of logic gates may be constructed. The surface normal output can be eliminated by design to obtain highest efficiency or could be retained to monitor circuit performance.

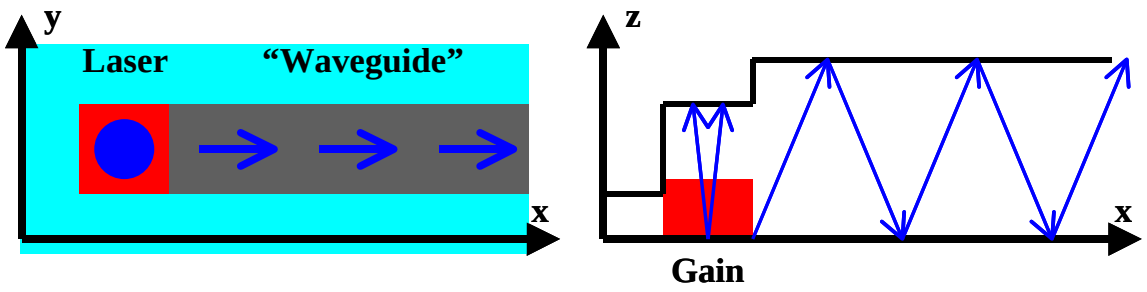

Figure 1.1. (a) Top view of wafer. Laser light (blue) leaks laterally from the active laser gain region (red) into the waveguide region (gray), by virtue of the waveguide region having a higher effective index (longer vertical cavity length) than the laser region. (b) Simplified cross-sectional view of the vertical cavity and the propagating light "rays".

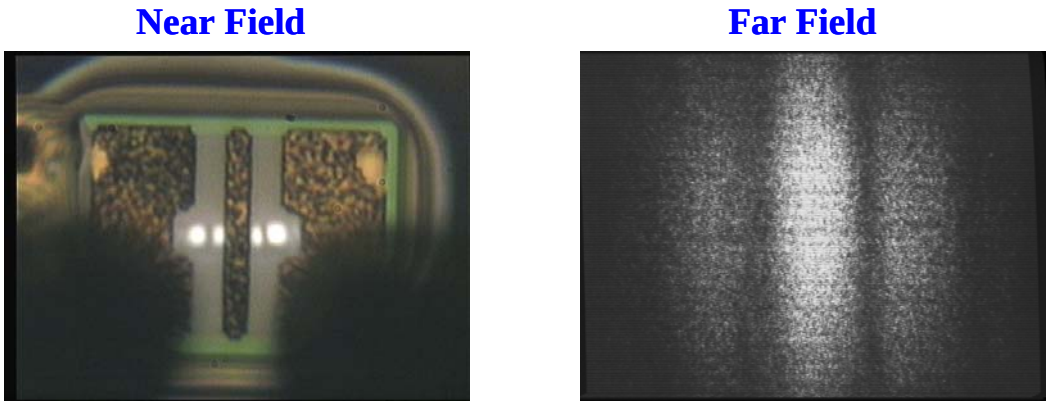

Figure 1.2. (a) Top view of two coupled VCSELs separated by an 8-micron-long channel. Because the system is symmetric, light propagates to both the left and right in the channel, and sets up a standing wave interference pattern. (b) Far-field image demonstrates that the two VCSELs are phase locked with a 0-degree phase difference.

One type of microcavity laser logic that we propose to investigate is based on the frequency shifting "optical diode" concept, illustrated in Figure 1.3(a). Photons originating in laser 1 can propagate into a higher effective index region, such as laser 2, but the reverse process is forbidden. The channel connecting laser i to laser i+1 together with laser i+1 is fabricated using a slightly increased cavity length so that its effective index is increased relative to laser i. Since light can move to higher index by tilting its propagation vector slightly but still remain on a Fabry-Perot resonance, the free-running mode of laser i can leak into the cavity of laser i+1 and quench its free-running mode. However, light attempting to cross into a region of lower index of refraction is reflected, and so laser i+1 can have no effect on the free-running mode of laser i. This makes an effective "optical diode" which inherently provides reverse isolation. As the cavity length is increased at each gate, eventually the next longitudinal mode is approached. When this happens, the cavity length for the next gate is returned to the starting value. From an effective index point of view this still appears as an index increase and so the operation of this gate is identical to the previous ones. The use of this longitudinal mode "wrap-around" technique satisfies cascadeability while at the same time limiting the complexity of the fabrication process.

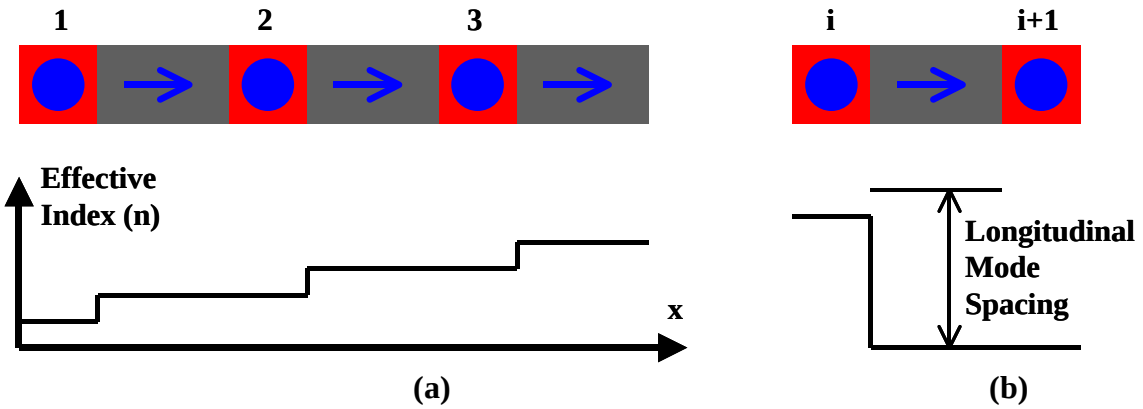

Figure 1.3. (a) Frequency shifting inverters. Each inverter is an "optical diode", where light can flow only in one direction. (b) How to force the frequency back to its starting point.

We also propose to investigate frequency degenerate logic gates as an alternative to the frequency shifting logic gates proposed above. Frequency degenerate optical logic gates rely on spatially overlapping modes of a microcavity that have identical frequencies but can be distinguished based on their lateral propagation vector components. Figure 1.4 shows a schematic top view of a microcavity that supports the frequency degenerate modes shown in Figure 1.4(a) and (b). Current is injected asymmetrically into the gain region (red), such that mode A is normally biased above threshold, and mode B is normally biased below threshold. Optical injection into mode B, by either the upper or lower waveguide channels, shown in gray in Figure 1.4, will quench the gain of mode A and suppress lasing. Hence, the mode A output that is coupled into the left and right waveguide channels, shown in gray in Figure 1.4, is an inverted function of the input into mode B. Since there are two inputs into mode B, either of which will suppress lasing in mode A, this element can function as a NOR gate.

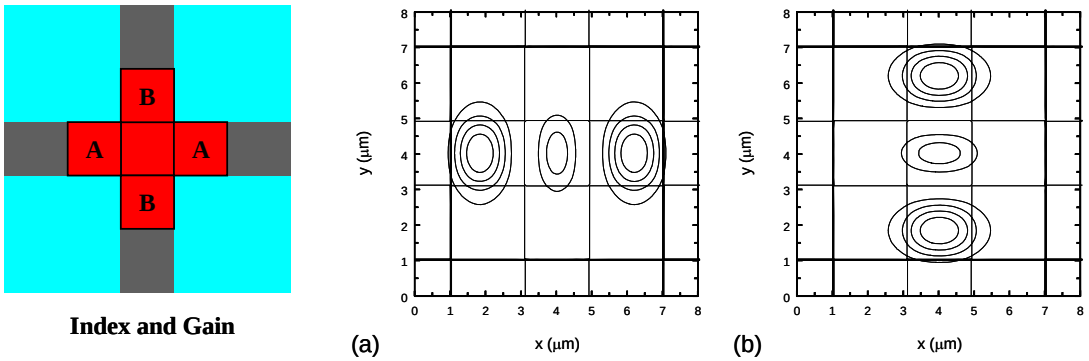

Figure 1.4. Top view of waveguide channels (gray), laser gain regions (red), and frequency degenerate laser modes. (a) Mode A is normally lasing, due to asymmetric gain (not shown), and emits light into the left and right output waveguide channels. (b) Mode B is always below threshold, but can be excited by external injection from either the top or bottom input waveguide channels.

2. Leaky Mode VCSEL Fabrication

2.1. Leaky Mode VCSEL Structure

Leaky mode VCSELs are different from standard VCSELs in that the effective index of refraction is decreased in the region where the laser mode is localized.[1,2] In a standard VCSEL light is confined within a high-index "core" region by an effect similar to total internal reflection in an optical fiber waveguide.[3] In a leaky mode VCSEL the "core" index is reduced relative to the "cladding". There is still a reflection at the core/cladding interface which tends to confine the light within the core, but because the reflection is not 100% some light tends to leak into the "cladding" region. Hence, these lasers are called "leaky mode" VCSELs.

It is relatively easy to produce a high index core region surrounded by a low index cladding region by etching a circular mesa through the VCSEL quantum well active region and placing the wafer in an oven containing a steam atmosphere in order to selectively oxidize one or more Al.98Ga.02As layers (n=3.0) to form aluminum oxide

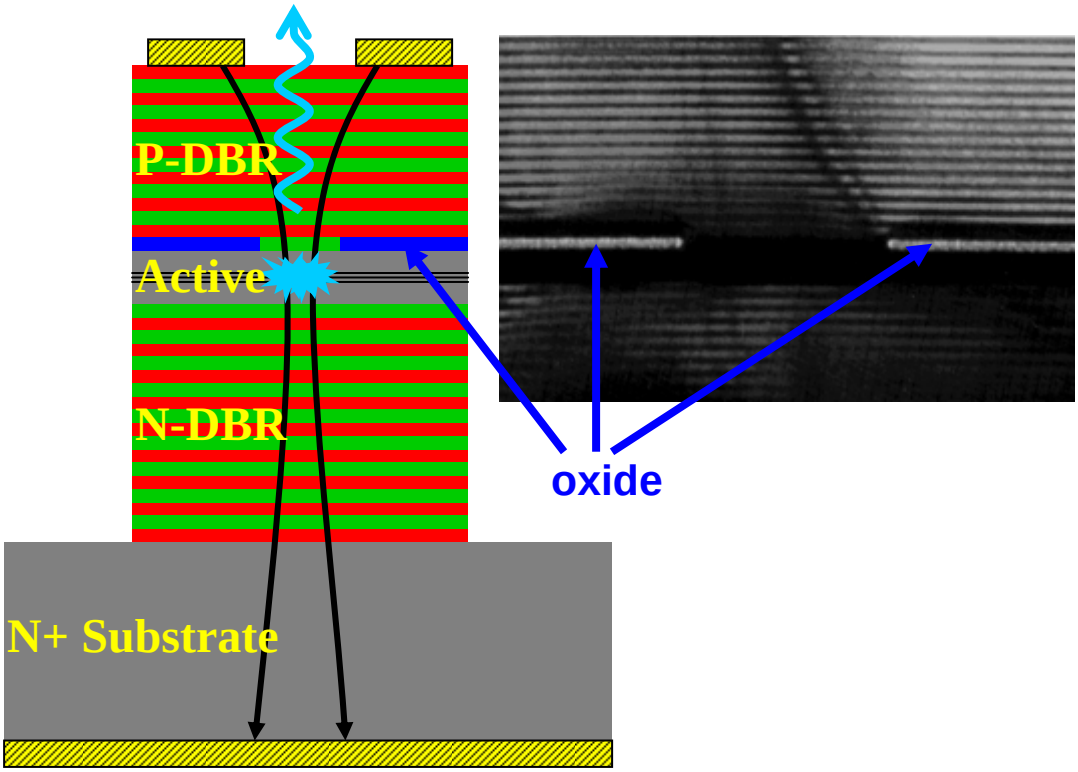

Figure 2.1. Cross-sectional schematic of a selectively oxidized VCSEL and a cross sectional SEM image of the same structure. The layer immediately above the active region is Al.98Ga.02As (n=3.0) and thus oxidizes significantly faster than the other layers of the DBRs which are Al.92Ga.08As and Al.16Ga.84As. The oxide (n=1.6) is colored blue in the drawing. The SEM image was produced by D. Mathes and R. Hull at the Univ. of Virginia.

(n=1.6), as shown in Figure 2.1. Our intuition correctly suggests that the low-index oxide layer reduces the effective index in the cladding region and gives rise to low-loss index-guided modes confined within the core (un-oxidized) region. In this case, the effective index in the core is 3.26 and the effective index step from the core to the cladding region is -0.06.

In 1995, G.R. Hadley made the profound observation that the effective index in any particular region (at lateral coordinates x and y) is determined by the vertical resonance wavelength in that region.[4] Thus, one can change the effective index either by (1) changing the permittivity of a layer or by (2) changing the thickness of a layer. While the first method is intuitive as illustrated in the previous paragraph, the second method is not so obvious. To illustrate with an extreme example, consider two gold plates that bound an air-gap cavity of length 850 nm. If we can somehow decrease the air gap length in a cladding region to 834 nm, then vertically propagating light near 850 nm will be confined to within the core region exactly as in the oxide confined VCSEL of the previous paragraph.

Hadley suggested that by laterally patterning the thickness of one or more layers in a VCSEL structure, we can arbitrarily control the effective index profile versus x and y. In particular, an index-guided VCSEL (similar to the oxidized VCSEL described above) can be fabricated by thinning one layer of the VCSEL structure throughout the cladding region only. Alternatively, an index anti-guided (or leaky mode) VCSEL can be fabricated by thinning one layer of the VCSEL structure within the core region only.[1,2]

A three-step process is required to obtain the effective index changes necessary for leaky-mode VCSELs as shown in Figure 2.2. Step 1: epitaxially grow roughly 60% of the VCSEL, including the bottom distributed Bragg reflector (DBR), the quantum-well optical gain region, and a few periods of the top DBR. Step 2: remove the wafer from the growth reactor, pattern openings in a mask, and perform a shallow etch of the un-masked semiconductor material. Step 3: return the wafer to the growth reactor and “regrow” the remainder of the top DBR.

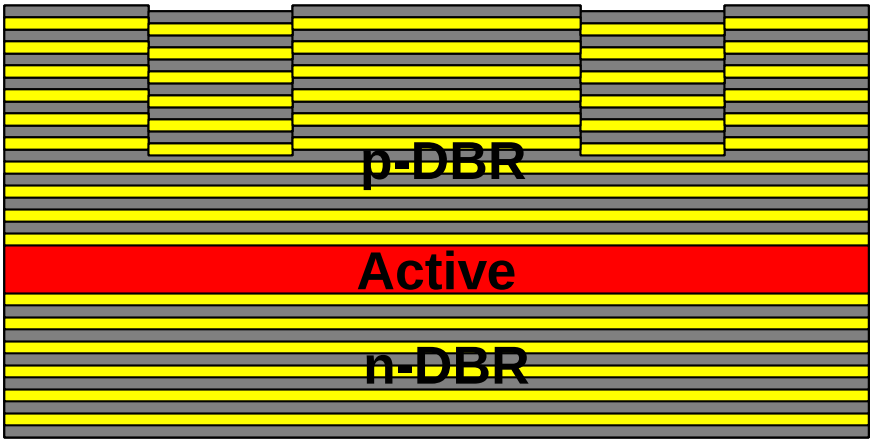

Figure 2.2. Cross sectional schematic showing 2 regions within which a layer in the p-type DBR has been etched before the remainder of the p-DBR is deposited.

The regions that were etched experience a slight blue shift of their micro-cavity resonance frequency, which acts equivalently to a decrease in the effective index of refraction. The details of these fabrication steps are discussed in the following sections.

2.2. Leaky Mode VCSEL Fabrication

One historic difficulty in fabricating leaky mode VCSELs was that of obtaining a precisely controlled shallow etch depth on the order of 10 nm. We have developed a new etching technique involving repeated cycles of oxidation and removal of the surface oxide, which allows us to precisely remove 2.25 nm of GaAs per cycle. Figure 2.3 shows the results of (a) 0 etch cycles, (b) 4 etch cycles, and (c) 8 etch cycles. The observed shift of the resonance wavelength corresponds closely to simulations, giving us confidence in our ability to do precise shallow etching. As an alternative, we have also exploited epitaxial growth of thin layers of materials such as InGaP that can be selectively etched with various dry and wet etch chemistries. Both of these chemically self-limited etch-back approaches afford us the controls necessary to confidently fabricate leaky-mode microcavity devices for a variety of applications

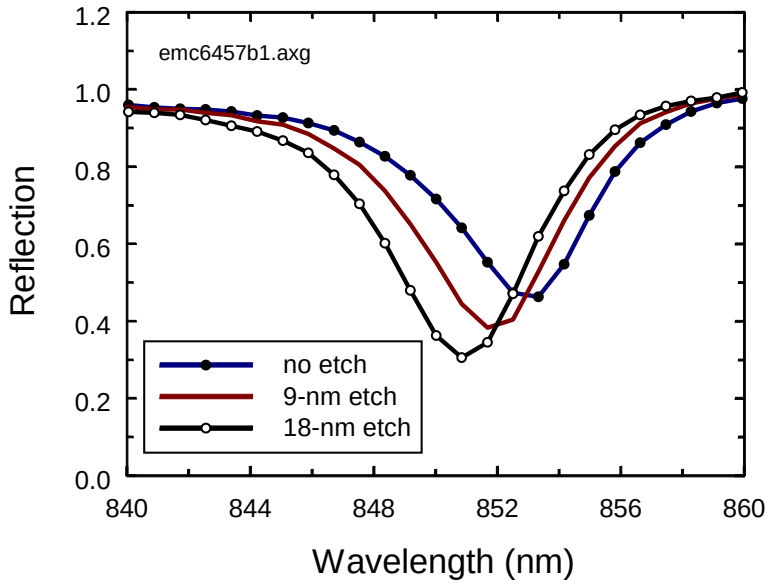

Figure 2.3. Reflection spectrum near the microcavity resonance dip after (a) 0 etch cycles, (b) 4 etch cycles, and (c) 8 etch cycles. The resonance dip appears broad because this VCSEL has only a partial top DBR.

Figure 2.4 shows a leaky-mode VCSEL fabricated using the oxidize/etch technique described above. This particular leaky-mode VCSEL represents the first step in an investigation of leaky-mode "waveguides" designed to route optical signals within a wafer. This leaky-mode VCSEL has been fabricated to output light horizontally, to the left in Figure 2.4. As discussed later, theoretical simulations of the optical spectrum have

been used to provide insight into the best ways to quantitatively measure the device performance for comparison with theory.

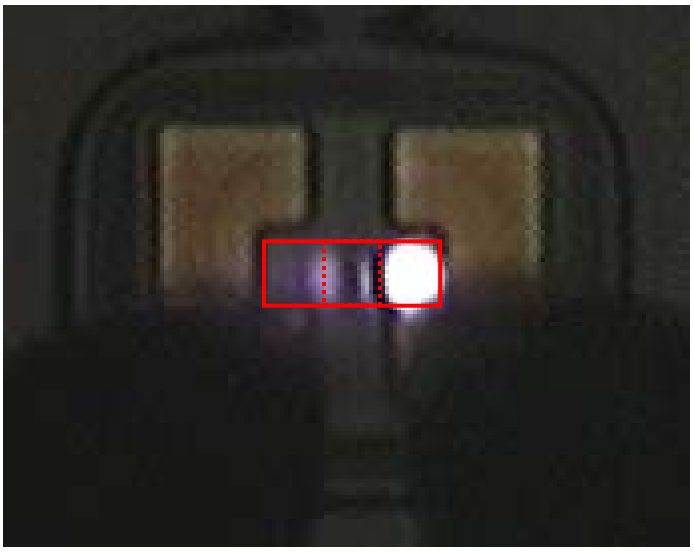

Figure 2.4. Top view of a leaky-mode VCSEL fabricated using our oxidize/etch technique. The VCSEL emits light into a leaky-mode "waveguide" on its left side. The solid red rectangle shows the boundary of the waveguide. The dotted red lines show the effective index steps. The standing wave pattern observed to the left of the VCSEL indicates that there is a significant lateral reflection coefficient from the effective index steps.

Regarding the implementation of the patterned etch step 2 of the leaky-mode VCSEL fabrication process, we found that etching through a patterned photoresist mask was not consistent enough. Instead, we pattern a thin layer of AZ 5214 photoresist (using a mask with the opposite tone of the one for creating a photoresist etch mask), then we deposit 20 nm of Ti and liftoff the Ti from above the photoresist regions. Moreover, the sample is rotated during the Ti deposition to eliminate shadowing by the photoresist. When the sample is removed from the evaporation chamber the Ti oxidizes to become TiO2. Thus, we have a TiO2 etch mask for subsequent selective wet chemical etching. We have typically used 1:4:495 H2PO4:H2O2:H2O to etch AlGaAs materials at 0.5nm/s and selectively stop on InGaP. We have used pure HCl to etch InGaP and selectively stop on AlGaAs. After the semiconductor etching is finished, we remove the TiO2 mask by etching in 1:100 HF:H2O for 2min.

We spent much effort on step 3 of the leaky-mode VCSEL fabrication process, namely the completion of the deposition of the top DBR. Although MOVPE growth of AlGaAs materials is typically done on GaAs substrates that are cut 2-degrees off axis, we have found that these substrates are not desirable for regrowth on etched features. The reason is that the discontinuities at the edges of the etched regions tend to propagate along the direction of the wafer miscut during the epitaxial regrowth step. This behavior is shown in Figure 2.5. The dark/rough area of the picture in Figure 2.5(a) shows amorphous deposition of AlGaAs on a region of the TiO2 mask that was intentionally left in place. Cross sectional SEM images have confirmed that the edges of the amorphous region are the same as the underlying TiO2 layer. Hence, the linear features within the amorphous

region show the original location of the etch pattern. Notice that in the epitaxial regrowth regions (at the top and left sides of the picture), the features have shifted significantly.

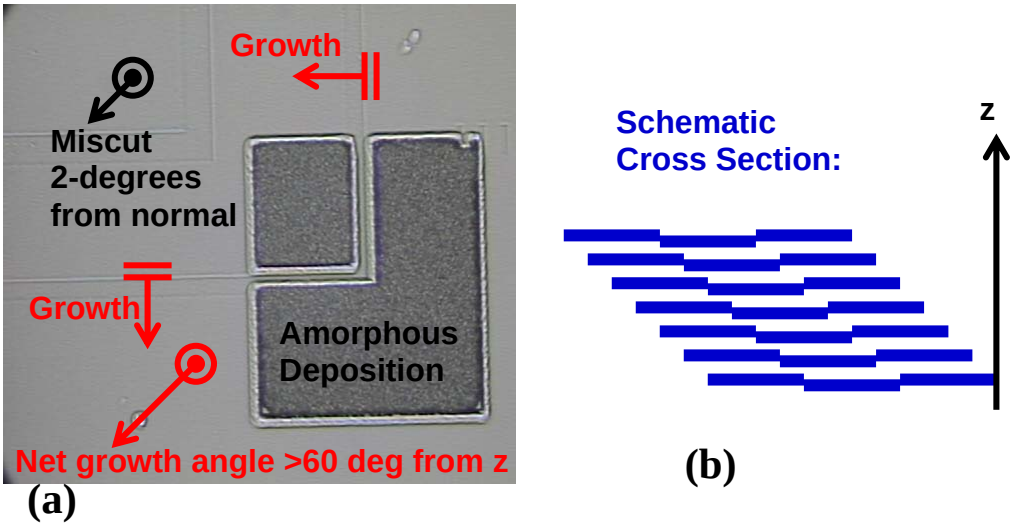

Figure 2.5. (a) Microscope image of epitaxial regrowth and amorphous semiconductor deposition on TiO2 (dark region). The relative shift of the vertical and horizontal trenches between the epitaxial and amorphous regions indicates that the regrowth occurs at a steep angle indicated schematically in (b).

Due to the undesirable regrowth angle shown in Figure 2.5, we have switched from using semiconductor wafers that are cut 2-degrees off axis to using wafers that are cut precisely along crystal planes. This change has required us to optimize growth on vicinal (100) gallium arsenide substrates, rather than the 2-degree miscut substrates that are conventionally used to provide nucleation sites for low-defect crystal growth.

As an alternative to epitaxial regrowth of the top DBR, we have deposited an amorphous dielectric SiO2/SiN DBR using the PlasmaTherm 790 PECVD tool. In support of this effort, we have modified the PlasmaTherm 790 wiring and recipes so that an external computer can independently control the deposition time of each layer in the DBR. Since a typical dielectric DBR consisting of 16 layers takes roughly 8 hours to deposit, it is a significant advance to have the process automated rather than requiring someone to stand by the machine for 8 hours. Figure 2.6 shows the transmission spectrum of a dielectric 980-nm DBR that was deposited using the new automation system. The 980-nm DBR spectrum is only intended to illustrate the typical dielectric DBR performance, but the actual DBRs deposited onto leaky mode VCSELs were centered at 850 nm. A simulation of an 850-nm DBR reflection spectrum is shown in Figure 2.7. We note that the upgrade of the PlasmaTherm 790 to enable automated dielectric DBR deposition benefits other research projects in the CSRL besides just the leaky-mode-VCSEL LDRD project.

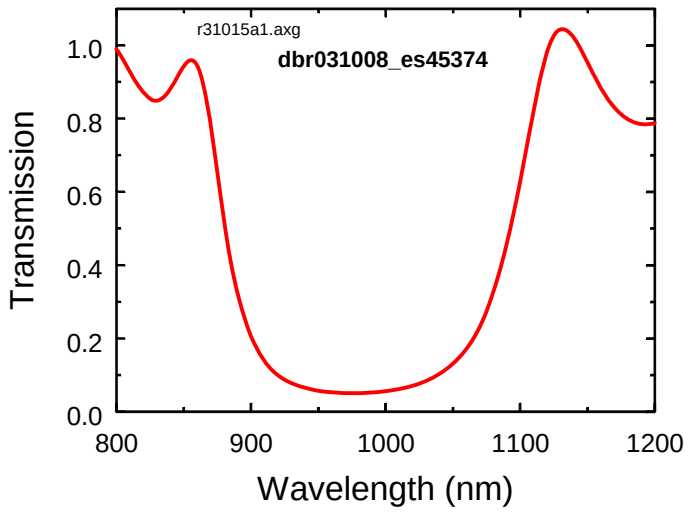

Figure 2.6. Transmission versus wavelength of a dielectric 980-nm SiO2/SiN mirror deposited in the PlasmaTherm 790 PECVD tool.

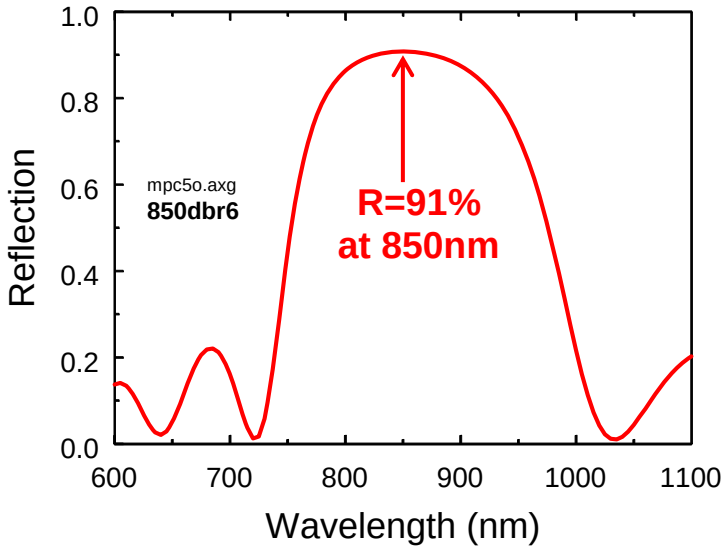

Figure 2.7. Simulated reflection spectrum of a 6-period dielectric SiO2/SiN DBR centered at 850 nm.

Having addressed the major fabrication issues associated with creating leaky-mode VCSEL devices, we turned our attention to the implementation of frequency shifting optical logic gates. Figure 2.8(a) shows a microscope image of a recently fabricated frequency-shifting all-optical NOR gate. The corresponding cross-sectional schematic is shown in Figure 2.8(b). The epitaxial structure is that of a standard 850-nm VCSEL, but with only a 6-period top p-type DBR. A quarter-wave Al.98Ga.02As layer in the first period of the p-type DBR was oxidized to create a current aperture, indicated by the 10-by-3-micron rectangle drawn in the center of Figure 2.8(a). In order to make a 2-element coupled VCSEL array, two 7-by-10-micron rectangles, barely visible in Figure 2.8(a), were etched to a nominal depth of 15 nm, removing the 10-nm GaAs cap layer and 5 nm of the 0.75-wave Al.16Ga.84As layer below it. An 8-period SiO2/SiN DBR was

deposited using plasma-enhanced chemical-vapor deposition (PECVD) using the PlasmaTherm 790 tool in the CSRL. The dielectric DBR was RIE etched from the perimeter of the mesa in order to provide access to the p-type ohmic contacts on top of the mesa. The n-type ohmic contacts were applied to the back side of the n-type conducting wafer number EMC7684.

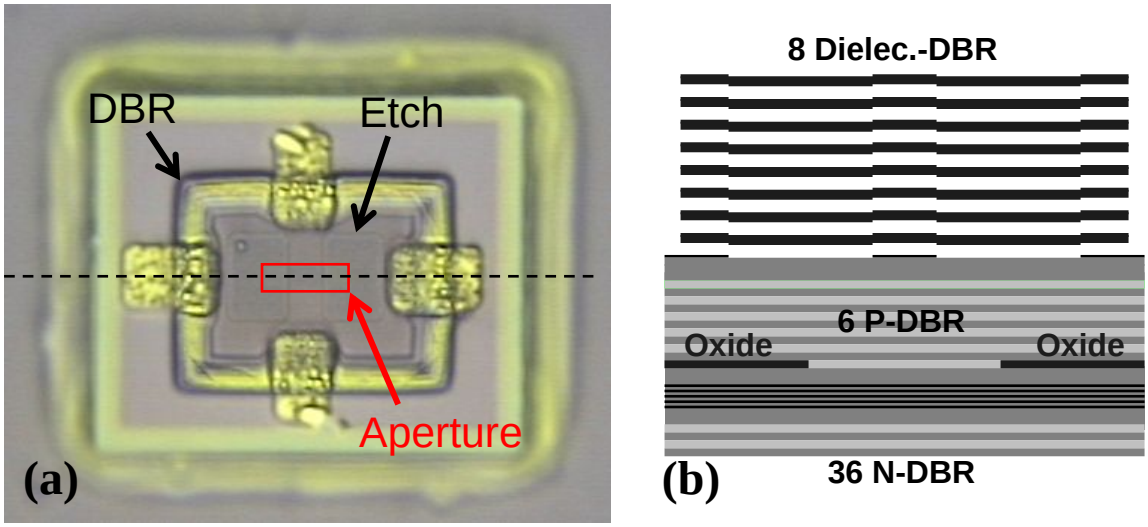

Figure 2.8. (a) Microscope image of the fabricated leaky mode VCSEL, showing the dielectric DBR, 2 shallow-etched rectangles, and a red rectangle indicating the edges of the oxide aperture (not visible). (b) Cross sectional schematic of the VCSEL layers.

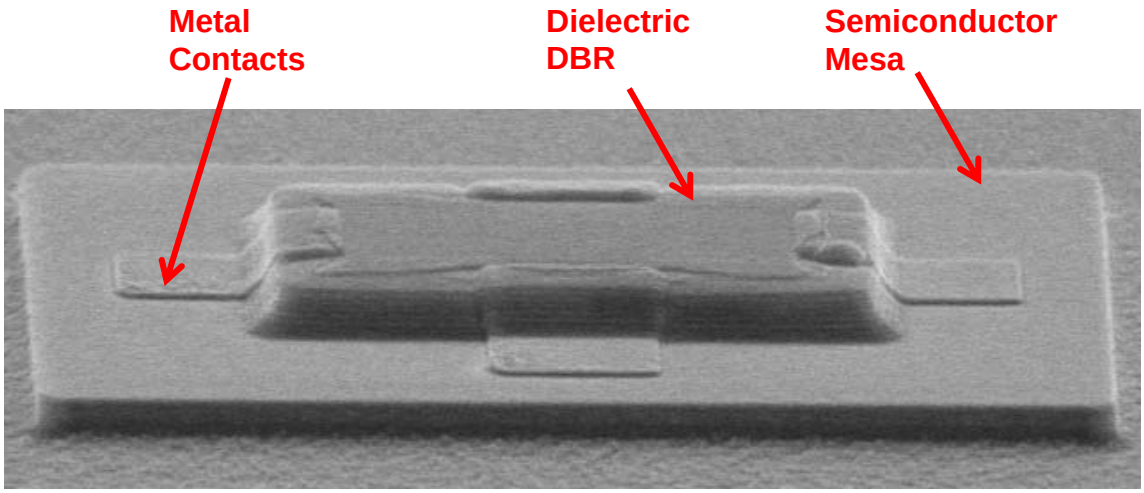

Figure 2.9. SEM image of the fabricated leaky mode coupled 1x2 VCSEL array.

Figure 2.9 shows a scanning electron microscope (SEM) image of the fully fabricated leaky mode coupled 1x2 VCSEL array. The top mesa shown in the image consists of the 8-period dielectric DBR, while the bottom mesa etch went through the 6 p-type DBR periods, the active region, and approximately 6 periods of the n-type lower DBR. Note that although the metal contacts are completely below the dielectric DBR stack, the

highly conformal deposition of the dielectric DBR preserves the 240-nm step defined by the p-type ohmic contact metal pads. A close-up SEM image of the VCSEL epitaxy and the lower and upper mesa etches is shown in Figure 2.10. The oxidized high-aluminum composition layers appear darker than the un-oxidized semiconductor layers.

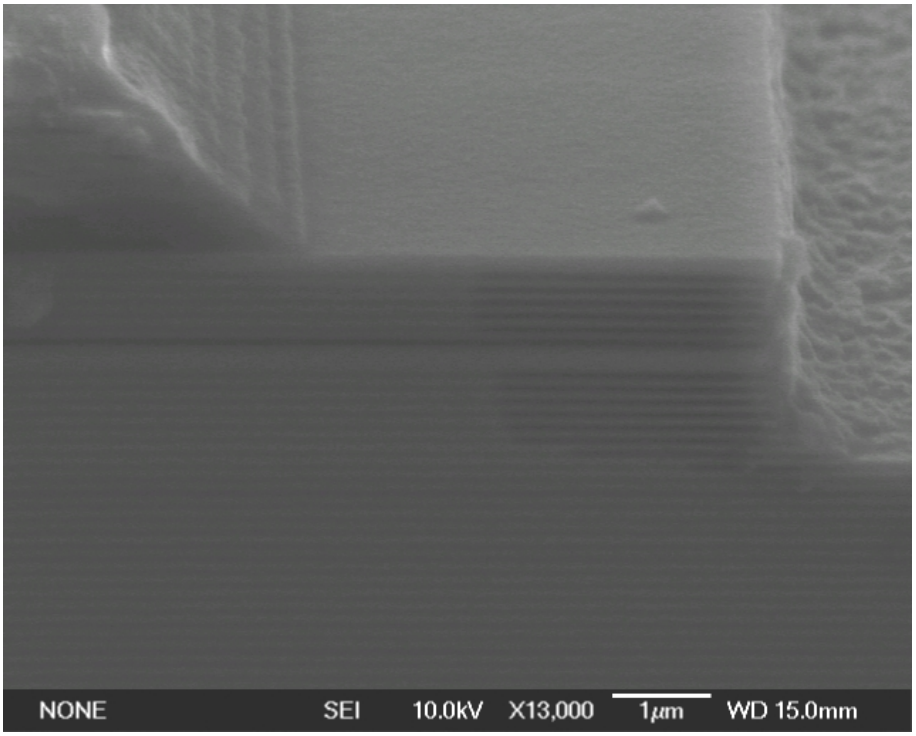

Figure 2.10. Close-up SEM image the VCSEL epitaxy and mesa etch.

3. Leaky Mode VCSEL Measurements and Modeling

3.1. Measurements: VCSELs with Dielectric Top DBR

While we had previously demonstrated 1x2 arrays of leaky mode coupled VCSELs using epitaxial regrowth of the top DBR,[5] in this section we present new results for leaky mode VCSELs fabricated using a dielectric top DBR. In particular, we will present results for the same device (EMC7684-A1B_306_N2_45_L4_20) that was described at the end of section 2.2. The VCSEL near-field output at 1.6 mA (above the 1.25-mA threshold of this device) is shown in Figure 3.1. The profile exhibits two primary lobes, one at each end of the oxide aperture. Between these two primary lobes, three dimmer secondary lobes appear within the 4-micron gap that separates the two etched regions.

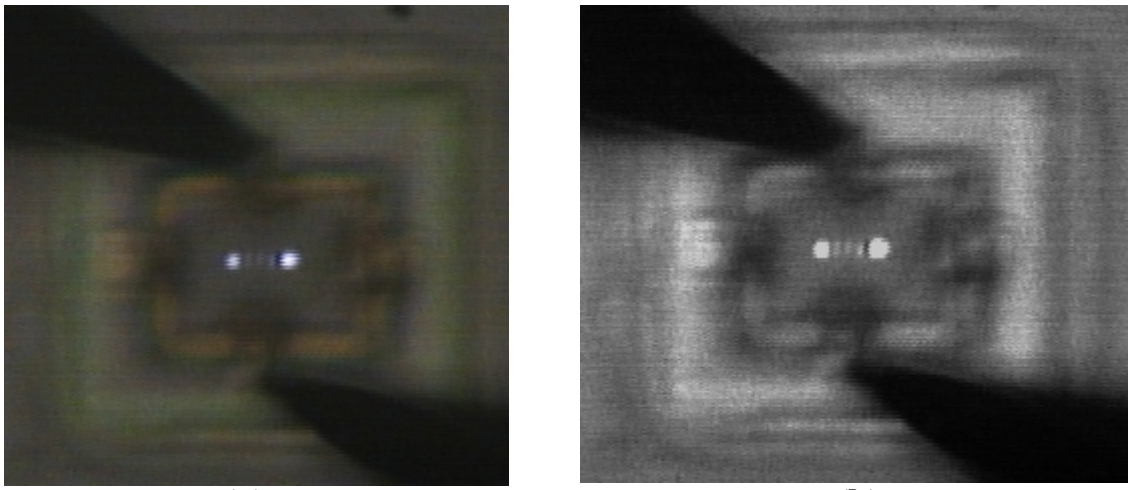

(a) **(b)**

Figure 3.1. (a) Color and (b) black-and-white near-field images of the VCSEL output at a drive current of 1.6 mA. The laser emission was selectively attenuated with filters to avoid saturation of the CCD camera.

Figure 3.2 shows both near-field and far-field images obtained at a VCSEL drive current of 1.5 mA (also above threshold). As in Ref. [5], the far-field measurements confirm a single on-axis peak indicating in-phase operation of the 2-element array. Note that although the three central lobes in the near-field image appear as bright as the outer 2 lobes, this is an artifact caused by CCD camera saturation. Figure 3.1 gives a more accurate view of the relative intensities of the various lobes. Whenever an odd number of intermediate lobes appear between the 2 outer VCSEL elements, the emission will be in phase. Whenever an even number of intermediate lobes appears between the 2 outer VCSEL elements, the emission will be out of phase. This behavior is a simple consequence of the fact that the optical phase flips by 180º from one lobe to the next all the way across a series of lobes (including the end lobes).

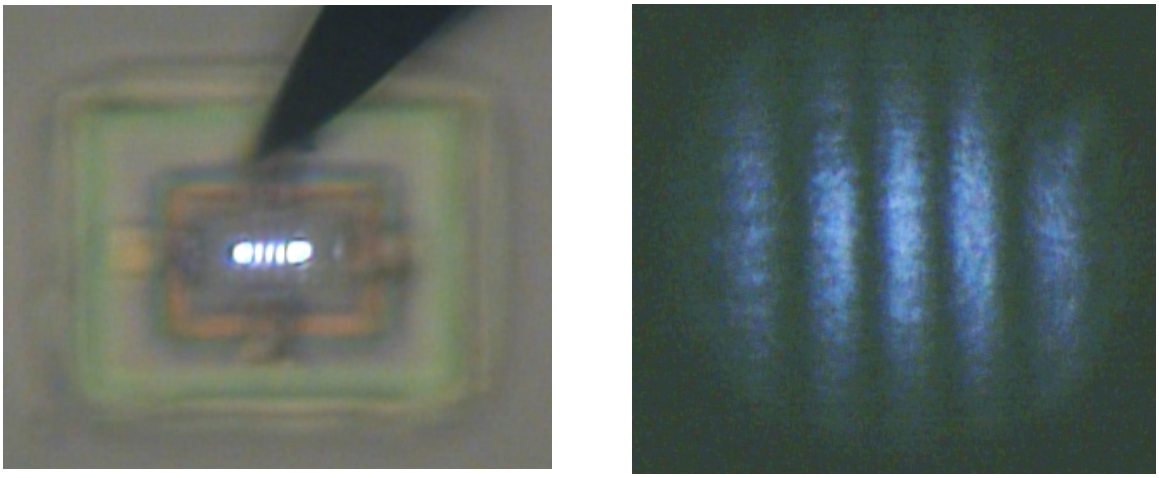

(a) **(b)**

Figure 3.2. (a) Near-field and (b) far-field emission profiles measured at a VCSEL drive current of 1.5 mA. Less attenuation of the laser emission was employed for these images, resulting in saturation of the CCD camera such that the three central lobes in the near-field image falsely appear as bright as the two outside lobes.

Figure 3.3 shows power and voltage versus current for this VCSEL, which reaches threshold at 1.25 mA. The output power is approximately 50% lower than a typical VCSEL having a similar oxide aperture area (3um x 10um) and the threshold current is surprisingly low. The top DBR reflectivity is calculated to be 99.8% versus 99.7% for a typical VCSEL, which helps account for the low threshold and the reduced output power. Another contribution to the reduced output power is likely the fact that the lasing mode only extracts power from a small fraction of the aperture area: namely from the two 3-micron diameter lobes at the two ends of the array.

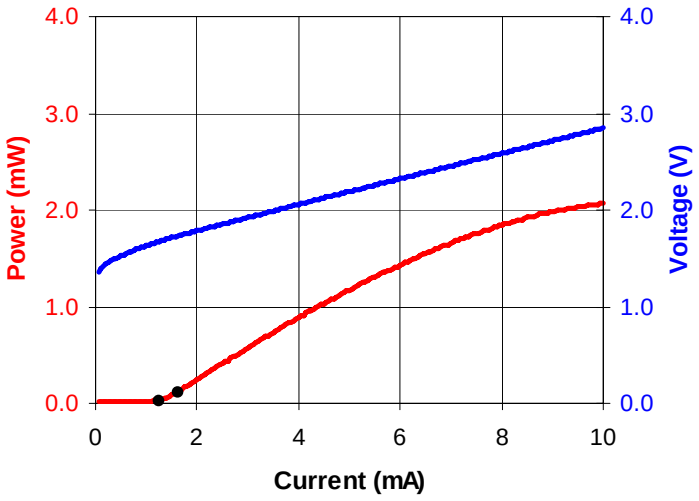

Figure 3.3. Power and voltage versus current for the leaky mode VCSEL device number EMC7684-A1B_306_N2_45_L4_20. The threshold current is 1.25 mA. Marker dots are shown at 1.2 mA and 1.6 mA, where spectra were recorded (see following section).

3.2. Spectral Theory and Measurements

Simulated mode profiles versus distance along the x-axis and corresponding mode wavelengths are shown in Figure 3.4 for the VCSEL discussed in the previous section. For the actual fabricated device, lasing of the fundamental mode, shown in red in Figure 3.4, was suppressed by the 10-nm GaAs cap that remained in the 4-micron-wide inter-element coupling region in the center of the device.

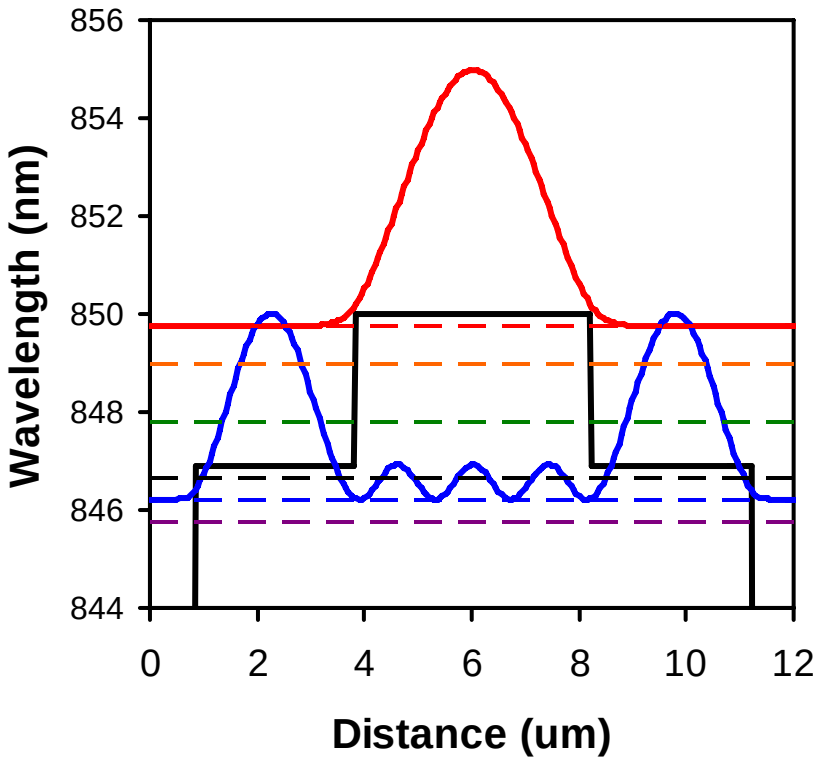

Figure 3.4. Simulated mode profiles versus the x-dimension and corresponding mode wavelengths for a leaky mode coupled VCSEL. The fundamental mode is shown in red and the higher-order lasing mode discussed in section 3.1 is shown in blue.

The VCSEL output spectrum is shown in Figure 3.5. The lasing spectrum (measured at 1.6mA) is shown in red and the below-threshold spectrum (measured at 1.2mA) is shown in blue (magnified vertically by 50 times to be more visible). Note that the longer-wavelength modes, which are spatially confined within the 4-micron-wide inter-element region, are clearly observed to be below threshold at a drive current of 1.6 mA. The reason is that the 10-nm thick GaAs cap layer remains on the 4-micron-wide inter-element region contributing additional optical absorption loss in this region.

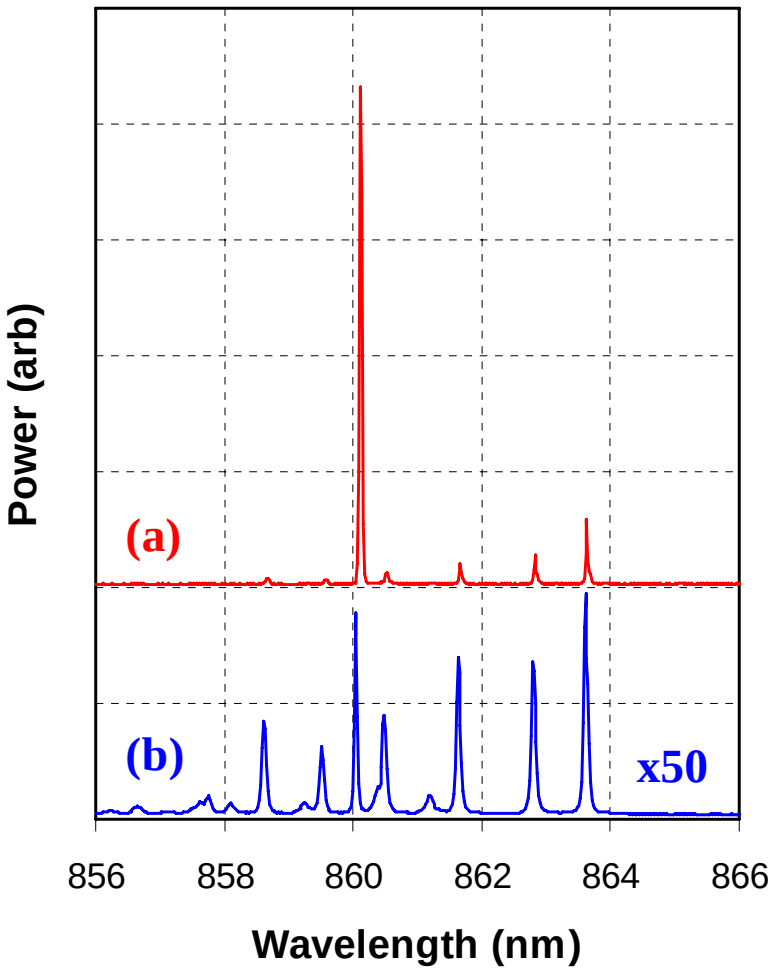

Figure 3.5. Emission spectra for the leaky mode VCSEL device number EMC7684-A1B_306_N2_45_L4_20, measured (a) above threshold (red) at 1.6 mA and (b) below threshold (blue) at 1.2 mA. The below threshold spectrum is vertically magnified by 50 times for visual comparison with the above-threshold spectrum.

The below-threshold emission spectrum can be compared to modal calculations done using effective index theory [3] in order to experimentally determine the actual fabricated dimensions. The assumed geometry for the modal calculations is shown in Figure 3.6. In order to simplify the calculations, we ignore the lateral dependence along the y-axis and focus only on the optical field variation along the x-axis. As shown in Figure 3.6, there are three types of regions to be considered: the oxidized region (light blue), the coupling region (pink) between the two VCSEL elements, and the two etched VCSEL elements (red). Each region is characterized by a vertical resonance wavelength that would be measured for an infinitely wide region. In Figure 3.6, nominal resonance wavelengths are indicated: 834nm in the oxidized region, 850nm in the etched regions, and 853nm in the coupling region.

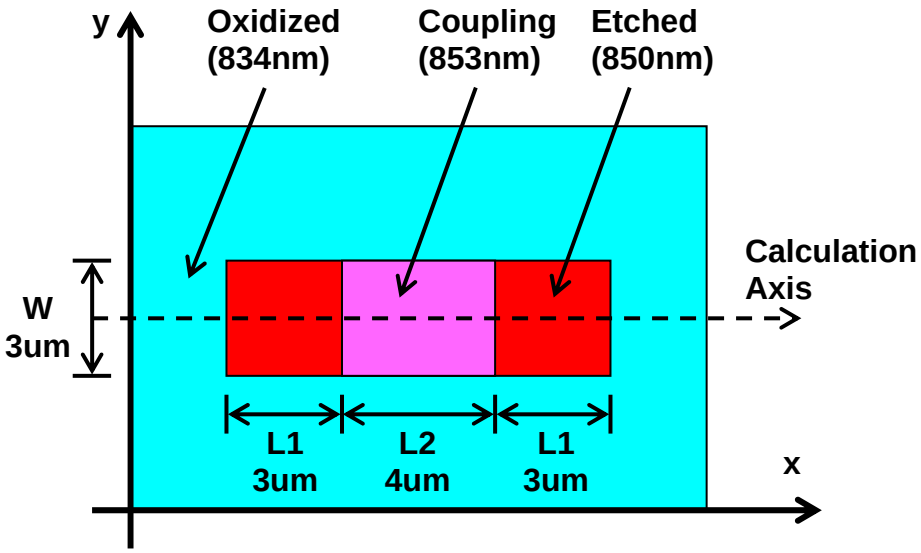

Figure 3.6. Schematic top view of the coupled VCSEL structure assumed for the effective index model. There are 3 regions of interest: the oxidized region (light blue), the semiconductor etched regions (red), and the coupling region (pink) that was not modified. Each region is characterized by a resonance wavelength (nominal values shown).

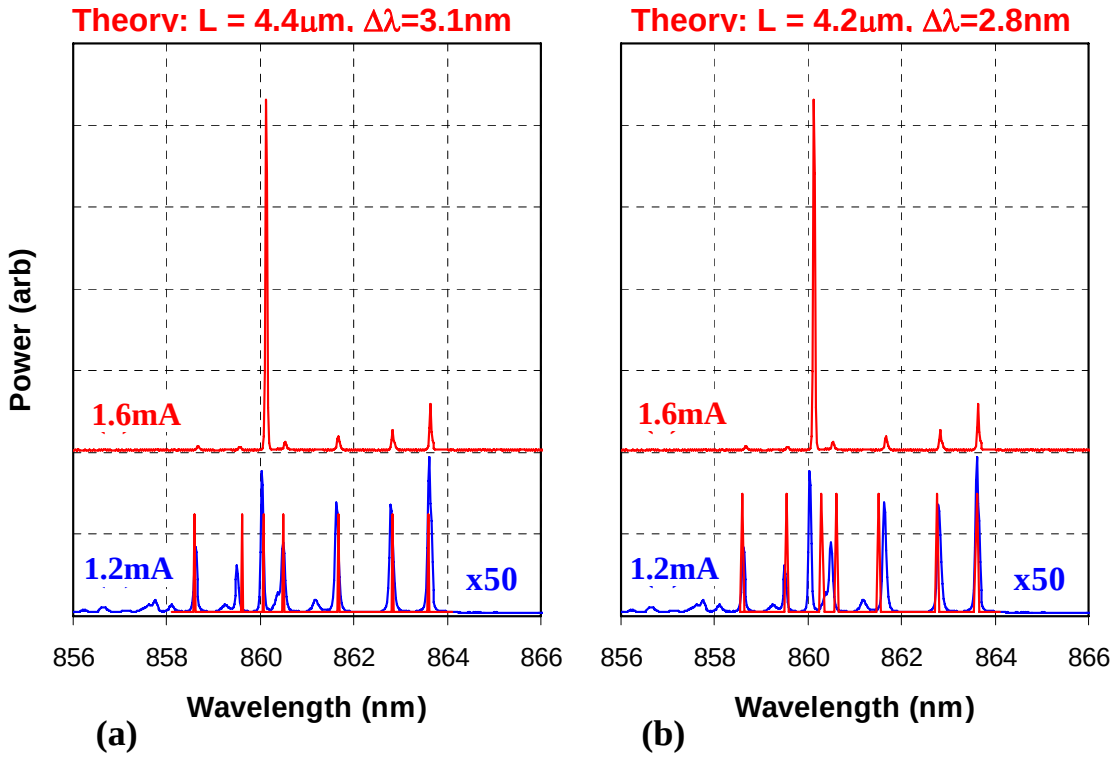

Figure 3.7. Comparison of below-threshold emission spectrum (blue) with theoretical calculations of the mode wavelengths (red equal-amplitude peaks) using an effective index model.

A series of calculations were performed to obtain the eigenvalues, $k_0 = 2\pi / \lambda_0$, of the equation

$$\frac{d^2 E_i(x)}{dx^2} + \langle \varepsilon_i \rangle (k_0^2 - k_{iz}^2) E_i(x) = 0, \qquad (1)$$

where in each region i the resonance wavelength λ_{iz} determines $k_{iz} = 2\pi / \lambda_{iz}$, and $\langle \varepsilon_i \rangle = 10.1$ approximately in all regions (see Ref. [3] for details). Typical simulation results (optical intensity profiles $I(x) = |E(x)|^2$ and modal wavelengths λ_0) were shown previously in Figure 3.4; also shown was the resonance wavelength profile $\lambda_z(x)$ (proportional to the effective index profile $n_{eff}(x)$) versus distance along the x-axis. In Figure 3.7 we compare the calculated modal wavelengths (equal amplitude red peaks) with those observed in the below-threshold spectrum (blue). The relative positions of the calculated modal wavelengths are most sensitive to the length L_2 of the inter-element coupling region and the relative resonance shift $\Delta\lambda = \lambda_{2z} - \lambda_{1z}$ between the etched region (λ_{1z}) and the coupling region (λ_{2z}). The best fit to the measured spectrum is obtained with L_2 = 4.4μm and $\Delta\lambda$ = 3.1nm, as shown in Figure 3.7(a). A small change of these parameters to L_2 = 4.2μm and $\Delta\lambda$ = 2.8nm yields a significant discrepancy with the measured spectrum, particularly with the position of the first mode that penetrates into the etched regions, as shown in Figure 3.7(b). The large sensitivity of the modal wavelength positions to the coupling region length L_2 and the relative resonance wavelength shift $\Delta\lambda = \lambda_{2z} - \lambda_{1z}$ allows us to accurately determine the actual fabricated length L_2 and the depth of the semiconductor etch, which is directly related (almost proportional) to $\Delta\lambda$. Thus, by measuring the laser spectrum below threshold we can determine the fabricated feature lateral widths to an accuracy of approximately 0.1μm and the etch depth to an accuracy of approximately 1nm.

3.3. VCSEL Gain Quenched Laser Logic

VCSELs are attractive candidates for high-speed gain-quenched laser logic devices [6,7] due to their short photon lifetime and the possibility of obtaining a large spatial overlap between the laser mode and the injected beam. The operation of a gain-quenched laser logic NOR gate will be briefly described here in order to understand appropriate conditions for the numerical simulations. A gain quenched laser, having optical modes similar to those shown in Figure 3.8, would be designed such that normally only the fundamental mode 1 (red) is above threshold. The higher order mode 2 (colored blue in Figure 3.8) would be designed to have a higher optical loss (for example, by reducing the number of top DBR periods over the two etched regions) so that it never lases. However, external light beams injected into either locations “In1” or “In2” in Figure 3.8 will resonate in the cavity and create a significant photon density in mode 2 (blue). Because mode 2 extends into the central coupling region where mode 1 exists, it will quench some of the gain being used by mode 1. If the quenching due to only one input is sufficient to

bring the lasing mode below threshold, then we have a NOR gate, since an input to either location “In1” or “In2” is sufficient to switch the output from ON to OFF.

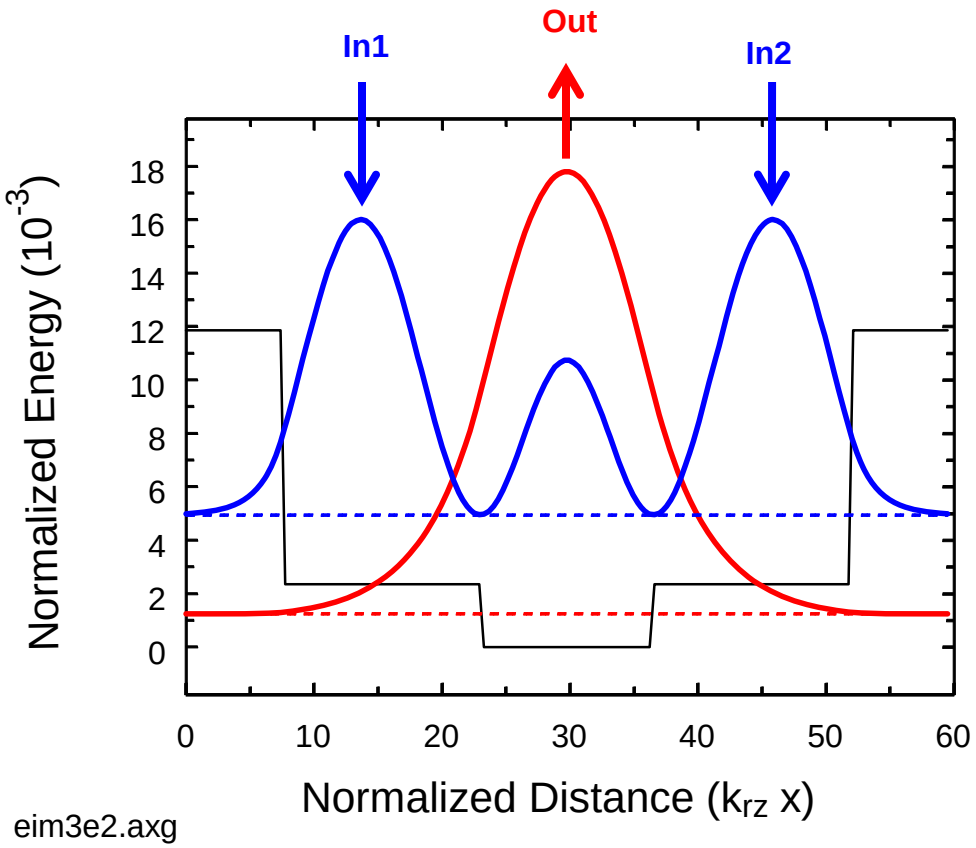

Figure 3.8. Modes 1 (red) and 2 (blue) of a leaky mode coupled VCSEL that could be used as a gain quenched laser logic gate. The laser would be designed so that only mode 1 (red) normally lases, by making a higher optical loss rate for mode 2 (blue). The normalized energy axis is determined by $V(x)=\frac{k_i^2(x)}{k_2^2}-1\approx\frac{2\Delta\lambda}{\lambda_2}$**, where** $\Delta\lambda=\lambda_2-\lambda_i(x)$ **and** λ_2 **is the resonance wavelength in the central coupling region.**

Next, we present rate equation simulations of gain quenched VCSEL dynamics in order to obtain an idea of the speed of response under various conditions. For simplicity, in order to understand the essential physics, we consider the situation where the spatial overlap between the lasing mode and the injected mode is 100%, which would occur for two TEM_{00} modes having orthogonal polarization states. The semiconductor laser rate equations,[8] for the carrier density N and photon densities S_1 and S_2 of the two optical modes under consideration, are

$$\frac{dN}{dt}=F-R-G(S_1+S_2), \tag{2}$$

$$\frac{dS_1}{dt} = \Gamma_1 G S_1 - \gamma_1 S_1, \tag{3}$$

$$\frac{dS_2}{dt} = \Gamma_2 G S_2 - \gamma_2 S_2 . \tag{4}$$

The forcing term $F = \eta_i I/qV$ gives the rate of carrier density increase due to injected current I into the active volume $V = L_A A_A$. For simplicity, we assume a carrier injection efficiency $\eta_i = 1$. The carrier recombination rate (without stimulated emission) is assumed to be dominated by spontaneous emission as $R = BN^2$, where $B = 0.8\times10^{-10}\,\mathrm{cm}^3/\mathrm{s}$ for GaAs quantum wells. We assume the stimulated emission rate depends on carrier density according to $G = v_g g_0 \ln(N/N_{tr})$, where $v_g = 0.9\times10^{10}\ \mathrm{cm/s}$ is the group velocity, $g_0 = 2400\mathrm{cm}^{-1}$ and $N_{tr} = 2.6\times10^{18}\,\mathrm{cm}^{-3}$ are assumed for a GaAs quantum well active region.[8] The confinement factors are determined by $\Gamma_j = \Gamma_{enh} V/V_j$, where $V_j = L_j A_j$ is the volume of an optical mode ($j = 1$ or 2), and we take $\Gamma_{enh} = 1.5$ to account for the enhancement due to the fact that the 5 GaAs quantum wells are located mostly within one peak of the longitudinal standing wave.[8] The areas A_A and A_j are assumed to be equal to $A = \pi(2\times10^{-4}\,\mathrm{cm})^2$. The total active length is $L_A = 0.04\times10^{-4}\,\mathrm{cm}$ and the optical mode lengths are both equal to $L_j = 1\times10^{-4}\,\mathrm{cm}$. The photon decay rates are assumed to be $\gamma_1 = 0.27\times10^{12}\,\mathrm{s}^{-1}$ for the lasing mode and $\gamma_2 = 0.54\times10^{12}\,\mathrm{s}^{-1}$ for the external optical input mode, which correspond to round-trip photon losses of 0.3% and 0.6%, respectively. The numbers quoted above yield a threshold current of 0.066 mA for optical mode 1, which is reasonable given our idealized assumptions: 100% carrier injection efficiency, no carrier recombination outside the active region volume, no mirror absorption or scattering losses, and a top mirror reflectivity somewhat higher than normal.

The rate equations described above were solved using a fourth-order Runge-Kutta method,[9] with equal time steps of 1 ps. In order to improve numerical stability, we forced the stimulated recombination term $G = 0$ when $N < N_{tr}$. In order to account for external optical input, the terms $\gamma_j S_j$ were replaced with $\gamma_j(S_j - S_{j0})$. Without any external input, the zero-point energy still results in $1/2$ photon per mode (which we insignificantly modified to 1 photon per mode in order to be visible on our logarithmic plots). The initial (at time zero) carrier density was taken to be $1\times10^{15}\,\mathrm{cm}^{-3}$, which is effectively zero, being far below transparency. The initial photon density, for each optical mode, was taken to be $1\times10^{14}\,\mathrm{cm}^{-3}$, which is roughly 2% of the lasing photon density. The simulation results are plotted in terms of the number of carriers, which is the product of the carrier density times the active region volume, and the number of photons, which is the product of the photon density times the volume of the optical mode.

A typical simulation result, for an injected current of 2 mA, is shown in Figure 3.9 , where the number of carriers is plotted on a linear scale and the number of photons is plotted on a logarithmic scale. Initially, the carrier density is far below the transparency density, and thus the photon numbers in the two optical modes are observed to decay at the rates γ_1 and γ_2 (according to our assumption the photon decay rate for mode 2 is twice the decay rate for mode 1). Initially, the carrier number builds up almost linearly due to the injected current. When the carrier density exceeds the transparency current density, the photon numbers start to increase from 1. At approximately $t = 180$ ps, mode 1 turns on and exhibits relaxation oscillations (at a frequency of 15 GHz) which are mostly damped by $t = 400$ ps. These results exhibit typical turn-on delays of 120ps for the carrier density to build up from zero and an additional 60ps for the photon density to build up from noise. Although the threshold for mode 2 alone is only 0.122 mA, the photons in mode 1 have quenched the gain sufficiently to prevent mode 2 from building up to a significant photon number.

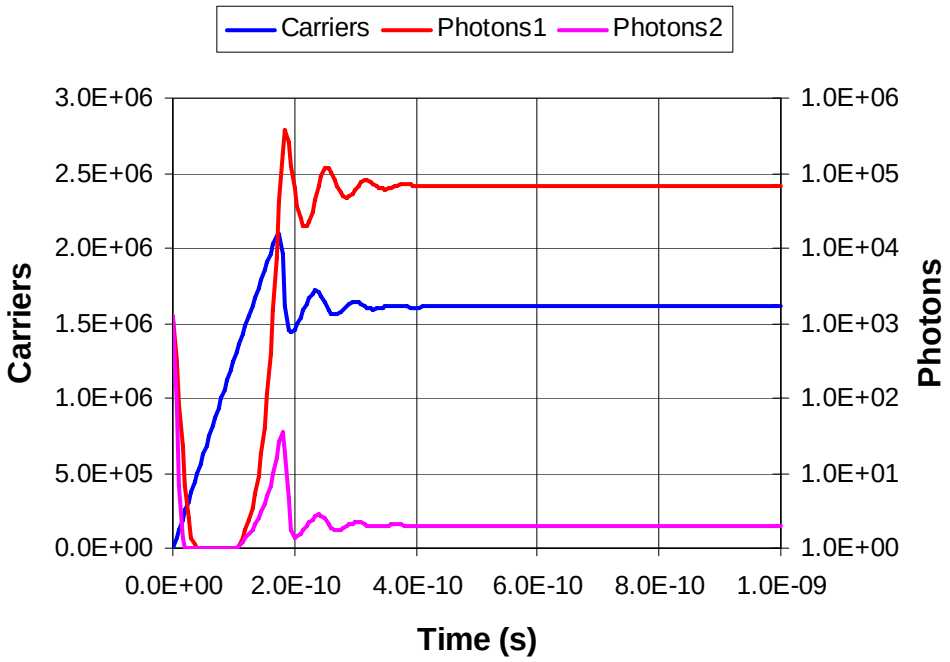

Figure 3.9. Simulated VCSEL rate equations with 2mA drive current and no input to optical mode 2. The carrier number scale is linear and the photon number scale is logarithmic.

Figure 3.10 shows the results of a second simulation, also with a 2-mA drive current, but with an externally injected 200-ps-long square pulse injected at $t = 500$ ps. The relaxation oscillations appear stronger than in the previous figure because the photon number is plotted on a linear scale, but the behavior before $t = 500$ ps is actually identical to that shown in the previous figure. The externally injected square pulse is assumed to have an abrupt rise at $t = 500$ ps and an abrupt fall at $t = 700$ ps. As observed in the figure, the cavity mode 2 does not respond instantaneously, but rather with a time

constant of $\tau_2 = \gamma_2^{-1} = 1.85$ ps. The amplitude of the injected pulse is chosen to produce 2×10^4 photons in mode 2 (30% of the number of photons in the free-running mode 1), in the absence of optical gain. Due to the available gain, we see in the figure that the injected pulse is amplified and results in 4×10^4 photons in mode 2 (60% of the number of photons in the free-running mode 1). Mode 1 (shown in red in the figure) is depleted 59% by gain quenching due to the photons circulating in mode 2. The fall time (10% to 90%) of mode 1 is approximately 15 ps and the rise time is approximately 10 ps, which correspond to approximately $1/2\pi$ times the period of the relaxation oscillation following each transition. In the situation where the output of a previous gain quenched laser provides the external input to mode 2, the response of mode 1 would be slowed a bit more. However, for the simulation conditions considered above, we can roughly estimate that the maximum NRZ operation frequency is potentially 2 times the relaxation oscillation frequency. For the results shown in Figure 3.10, the relaxation oscillation frequency is approximately 10 GHz in the low (quenched) state of mode 1, which implies a maximum logic operation frequency of 20 GHz.

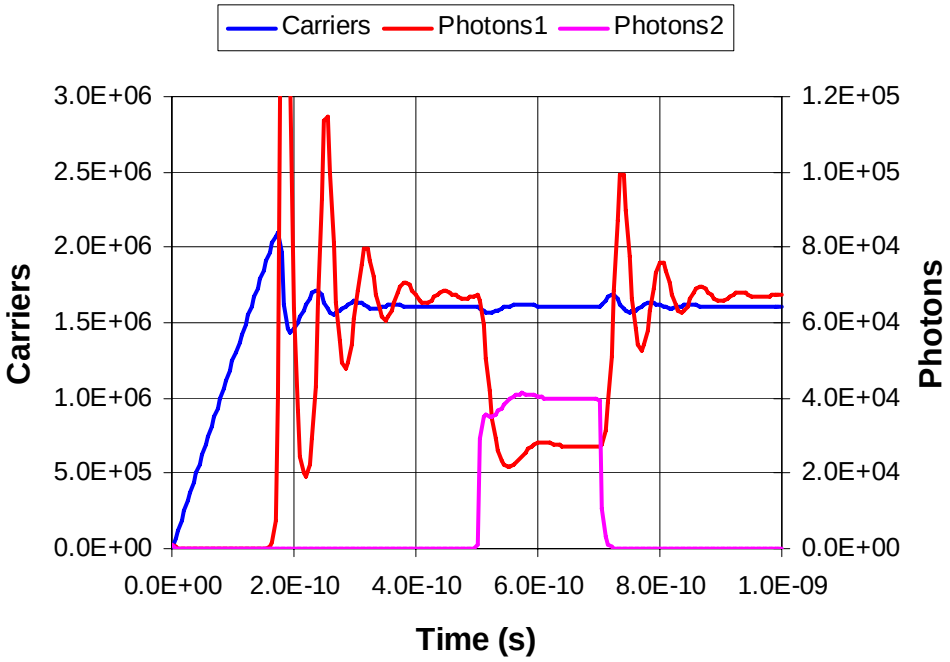

Figure 3.10. Simulated VCSEL rate equations with 2mA drive current, and external optical input to photon mode 2 at times from 500 to 700 ps. The results at times before 500 ps are identical to the previous figure, but both the carrier and photon scales are linear.

Figure 3.11 shows the results of a third simulation, which is identical to the previous one, except the amplitude of the injected pulse is chosen to produce 4×10^4 photons in mode 2 (60% of the number of photons in the free-running mode 1), in the absence of optical gain. Doubling the amplitude of the external optical input has completely quenched lasing mode 1. The most notable difference compared to the previous simulation is that

there is a roughly 40 ps delay time from when the mode 2 input falls to zero until the mode 1 amplitude returns to a high level. This result is expected, and explicitly shows that in order to maintain high-speed operation, gain-quenched laser modes should never be completely shut off. From a system level perspective, this suggests that NOR gates might always suffer long turn-on delays.

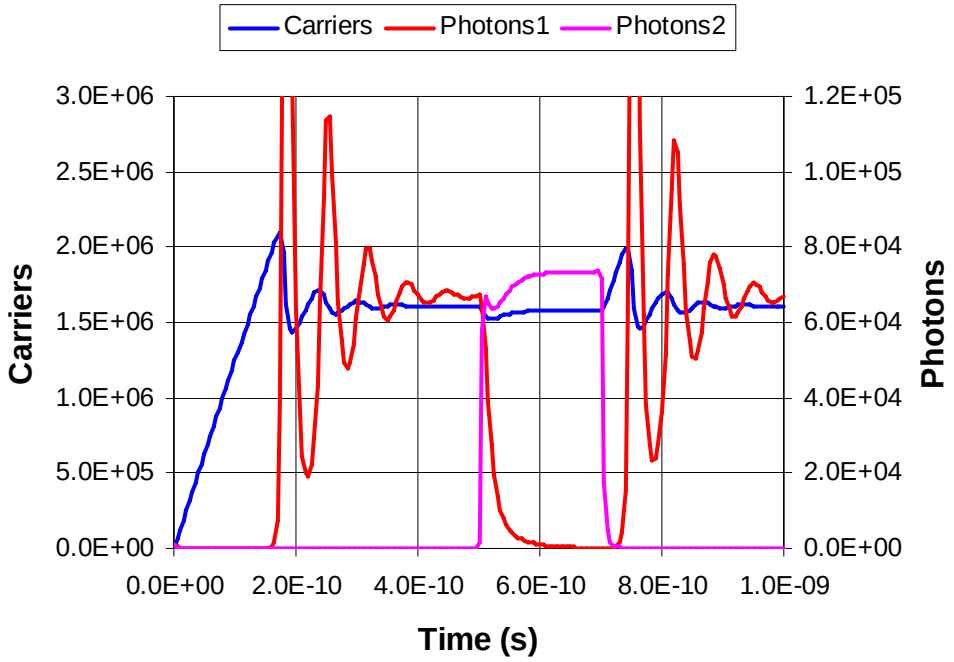

Figure 3.11. Simulated VCSEL rate equations with 2mA drive current, and an external optical input to photon mode 2 which is 2 times higher than in the previous figure.

Since the previous results suggest that we do not want to completely shut off the lasing mode 1, we next consider the situation in which the external optical input does not have a high extinction ratio, which is appropriate if that input came from another gain quenched laser that was not completely shut off. In particular, Figure 3.12 shows simulation results that are identical to those of Figure 3.10 except that the baseline injected photon level into mode 2 is half of the injection level during the 200-ps pulse. Because mode 1 is now partially quenched by mode 2 in the baseline state, the fractional quenching that occurs during the 200-ps pulse is only 44%, which is reduced from the value of 59% shown in Figure 3.10. This final simulation result is very close to what might be used in a real system. An even more realistic simulation, which is not attempted here, would take the actual output waveform of one gain quenched laser as the input to a second gain quenched laser. Thus, the abrupt-transition square pulse input would be replaced with an input pulse having roughly 15-ps rise/fall times and ringing following each transition. Nonetheless, the results presented in this section have provided significant insight into the dominant performance parameters of realistic gain quenched VCSELs.

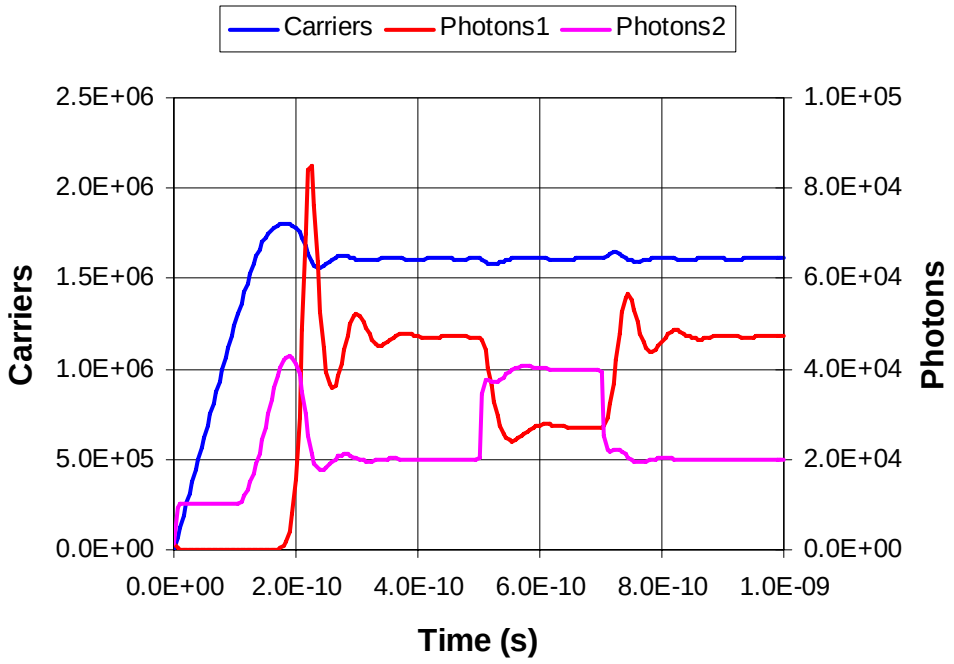

Figure 3.12. Simulated VCSEL rate equations with 2mA drive current, and an external optical input that varies from a baseline level of 1E+4 photons into mode 2, in the absence of optical gain, to 2E+4 photons between t = 500 and 700 ps.

4. Summary

During this 3-year LDRD we have significantly improved our ability to fabricate, characterize, and model leaky mode VCSELs. In particular, we have improved our ability to etch semiconductors to nominal depths of 20 nm with high accuracy in both the vertical and lateral dimensions. We have also explored a variety of AlGaAs semiconductor DBR epitaxial regrowth conditions and the use of various substrates, having different miscut orientation angles. Finally, as an alternative to epitaxial regrowth, we have deposited amorphous dielectric SiO2/SiN top DBRs to complete leaky mode VCSEL structures. The deposited dielectric DBRs have worked extremely well for making leaky mode gain quenched VCSELs. The only type of leaky mode VCSEL that may not work well with dielectric DBRs would be a large 2-dimensional array, in which case the high electrical and thermal resistance of the dielectric DBR could be a significant disadvantage.

Our ability to accurately characterize and model leaky mode VCSELs has also improved considerably during this LDRD project. In particular, we have measured the above-threshold and below-threshold emission spectra from leaky mode VCSELs and compared them with effective index model results. Such a comparison between the measured and simulated VCSEL spectrum has proven to be an excellent method of determining the fabricated feature lateral widths to an accuracy of approximately 0.1μm and the etch depth to an accuracy of approximately 1nm.

Rate equation modeling of gain quenched VCSELs has given us good insight into the expected response time and useful injection conditions required to achieve high-speed laser logic operation. The simulations suggest that for realistic VCSELs, photon-carrier dynamics limit the maximum NRZ bit rate to twice the relaxation oscillation frequency that is observed in the quenched state. Moreover, the simulations indicate that complete quenching of the free-running laser mode should be avoided due to the long time delays required to emerge from the fully quenched state. From a system level perspective, this suggests that NOR gates might never work well at high speeds.

This LDRD has partially supported the demonstration of a new approach to optical time-domain reflectometry (OTDR) that will enable distributed fault monitoring in single-mode VCSEL-based networks. In-situ OTDR uses the transmitter VCSEL already resident in data transceivers as both emitter and resonant-cavity photodiode for fault location measurements. Also valuable at longer wavelengths, the concept has been demonstrated using an 850-nm oxide-confined VCSEL and simple electronics. The dead times and sensitivity obtained are adequate to detect the majority of faults anticipated in local- and metropolitan-area networks. This work was published in Electronic Letters in July 2005.[10]

In collaboration with Daniel M. Grasso and professor Kent D. Choquette of the University of Illinois, we have measured the electrical bandwidth of coupled-cavity VCSELs in either single-mode or dual-mode operation. This work was presented at the 2004 LEOS Annual Meeting in November 2004 in Puerto Rico.[11]

In collaboration with Preetpaul Devgan and professor Prem Kumar of Northwestern University, we have demonstrated an optoelectronic oscillator using an 850nm VCSEL for generating low jitter optical pulses. A manuscript was submitted to Photonics Technology Letters in October 2005.

5. References

[1] T.-H. Oh, O.B. Shchekin, and D.G. Deppe, “Single-Mode Operation in an Antiguided Vertical-Cavity Surface-Emitting Laser Using a Low-Temperature Grown AlGaAs Dielectric Aperture,” IEEE Photon. Technol. Lett., vol. 10, pp. 1064-1066 (1998).

[2] K.D. Choquette, G.R. Hadley, H.Q. Hou, K.M. Geib, and B.E. Hammons, “Leaky mode vertical cavity lasers using cavity resonance modification,” Electron. Lett., vol. 34, pp. 991-992 (1998).

[3] D.K. Serkland, G.R. Hadley, K.D. Choquette, K.M. Geib, and A.A. Allerman, “Modal frequencies of vertical-cavity lasers determined by an effective-index model,” Appl. Phys. Lett., vol. 77, pp. 22-24 (2000).

[4] G.R. Hadley, “Effective index model for vertical-cavity surface-emitting lasers,” Opt. Lett., vol. 20, pp. 1483-1485 (1995).

[5] D.K. Serkland, K.D. Choquette, G.R. Hadley, K.M. Geib, and A.A. Allerman, “Two-element phased array of antiguided vertical-cavity lasers,” Appl. Phys. Lett., vol. 75, pp. 3754-3756 (1999).

[6] J. L. Fitz, W. T. Beard, S. C. Horst, and S. D. Smith, “Integrated Photonic Inverter with Gain,” IEEE Photon. Technol. Lett., vol. 13, pp. 478-480 (2001).

[7] D. B. Shire, C. L. Tang, M. A. Parker, P. D. Swanson, and J. S. Kimmet, “Gain controlled vertical cavity surface emitting lasers coupled with intracavity in-plane lasers,” Appl. Phys. Lett., vol. 66, pp. 1717-1719 (1995).

[8] L. A. Coldren and S. W. Corzine, *Diode Lasers and Photonic Integrated Circuits*, Wiley, New York (1995).

[9] W. H. Press, S. A. Teukolsky, W. T. Vetterling, B. P. Fannery, *Numerical Recipes in C: The Art of Scientific Computing, Second Edition*, Cambridge University Press, Cambridge (1992).

[10] G. A. Keeler, D. K. Serkland, K. M. Geib, G. M. Peake, “In situ OTDR for low-cost optical networks using singlemode 850 nm VCSEL,” Electronics Lett., vol. 41, pp. 819-820 (2005).

[11] D. M. Grasso, D. K. Serkland, K. M. Geib, K. D. Choquette, “High-speed characteristics of composite-resonator vertical-cavity lasers,” 2004 IEEE LEOS Annual Meeting Conference Proceedings, vol. 1, pp. 242-243, (Nov. 2004, Rio Grande, Puerto Rico, USA).

DISTRIBUTION:

8	MS	0603	D. K. Serkland, 1742
2		0603	C. T. Sullivan, 1742
1		0603	K. M. Geib, 1742
1		0603	G. M. Peake, 1742
1		0603	G. R. Hadley, 1742
1		0603	G. A. Keeler, 1742
1		0603	E. L. Blansett, 1742
1		0188	LDRD Program Office, 1030
2		9018	Central Technical Files, 8945-1
2		0899	Technical Library, 9616